

CHAPTER 81

DIRECTIONAL NEARSHORE WAVE PROPAGATION AND INDUCED CURRENTS

M.W. Dingemans,¹⁾ M.J.F. Stive,¹⁾ J. Bosma,¹⁾
H.J. de Vriend¹⁾ and J.A. Vogel²⁾

ABSTRACT

Recently, a depth and current refraction model has been developed for the computation of directionally spread, random wave propagation in coastal regions (Booij et al., 1985). For the verification of the performance of this model laboratory measurements in a directional, shallow water wave basin were conducted. Specific attention was given to the verification of the new features of the numerical model, viz. the effects of directional spreading and ambient current field on the wave propagation and transformation process, and the change of characteristic spectral wave frequency due to wave dissipation processes.

1.0 INTRODUCTION

Since the late seventies it has become a policy in the Netherlands to verify the performance of nearshore wave propagation models (see e.g. Dingemans et al., 1984). Recently, the Delft Technical University has devised a depth and current refraction model on a grid including directional characteristics, HISWA, see also Holthuijsen and Booij (1986) in these proceedings. In contrast to the now generally accepted parabolic refraction-diffraction models, for this model it was chosen to disregard the diffraction part in order to include directional spreading of the wave field. Moreover, also the change of characteristic wave period has been modelled. Because from the previous verification studies only scarce information on directional spread is available, a special laboratory experiment has been set up in a new wave basin, equiped to generate directional, shallow water waves (Mynett et al., 1984).

The primary purpose of this study is the verification of the wave heights and the wave periods, including the effect of directional spread on the wave characteristics. A geometry consisting of a semi-cylindrical bank on a horizontal bottom has been chosen, so that these effects may be studied.

In order to separate the two-dimensional effects around the tip of the bank, refraction and diffraction, from the one-dimensional effects due to shoaling and wave breaking, also the case of the fully cylindrical bar has been included. Moreover, to obtain information on the variability of the wave field in the basin, also the case of constant depth is considered.

Here a first, concise report is given of the verification of HISWA against the laboratory measurements. A full report will appear elsewhere.

1) Delft Hydraulics, Delft, the Netherlands

2) Rijkswaterstaat - DGW, den Haag, the Netherlands

2.0 MATHEMATICAL FORMULATION OF HISWA

It is well known that the evolution of random wave fields can be described by

$$\frac{\partial A}{\partial t} + \dot{x}_i \frac{\partial A}{\partial x_i} + \dot{k}_i \frac{\partial A}{\partial k_i} = S, \tag{1}$$

where $A(\vec{k}, \vec{x}, t)$ denotes the wave action density, $\dot{x}_i \equiv dx_i/dt = \partial\Omega/\partial k_i$ is the group velocity, v_i , and $\dot{k}_i \equiv dk_i/dt = -\partial\Omega/\partial x_i$ is the rate of change of wave number due to refraction. Notice that the summation convention has been used with $i = 1, 2$. The dispersion relation is given as $\omega = \Omega(\vec{k}, \vec{x}, t)$. When the medium in which the waves propagate does not depend on time explicitly, one has $\omega = \Omega(\vec{k}, \vec{x})$, which case is taken here; in that case Ω is a Hamiltonian for the vector field (\dot{x}_i, \dot{k}_i) . In the case of an ambient current field $\vec{U}(\vec{x})$ one has

$$\Omega = \omega_r + k_i U_i, \quad \omega_r = [gk \cdot \tanh kh]^{\frac{1}{2}}, \quad k = |\vec{k}|,$$

where $h(\vec{x})$ is the waterdepth. Then one has $v_i = c_{gi} + U_i$ and $c_{gi} = \partial\omega_r/\partial x_i$. Transforming from (k, x) space to the space (x, ω, θ) , with θ the wave direction, and introducing the absolute energy density \tilde{E} by $\tilde{E} = A\omega$, one obtains for the transport of energy along the vector field defined by the Hamiltonian Ω ,

$$\frac{\partial \tilde{E}}{\partial t} + \frac{\partial}{\partial x_i} [\tilde{E} v_i] - \frac{\partial}{\partial \theta} [\tilde{E} \{ (c_g - \frac{c}{2}) \frac{1}{h} \frac{\partial h}{\partial n} + \cos\theta \frac{\partial U_1}{\partial n} + \sin\theta \frac{\partial U_2}{\partial n} \}] = \omega S, \tag{2}$$

where $c = \omega_r/k$ and n is the direction in space normal to θ . This equation for the absolute energy becomes, after assuming time-independency ($\partial\tilde{E}/\partial t \equiv 0$, and thus stationary wave fields) and integration over ω between 0 and ∞ :

$$\frac{\partial}{\partial x_i} [\omega^{(A)} \cdot A^{(o)} \cdot \bar{v}_i] + \frac{\partial}{\partial \theta} [\omega^{(A)} \cdot A^{(o)} \cdot \bar{C}_\theta] = S_1, \tag{3}$$

where the mean quantities $\omega^{(A)}$, $A^{(o)}$, \bar{v}_i and \bar{C}_θ are defined by

$$\begin{aligned} A^{(o)}(\vec{x}, \theta) &= \int_0^\infty A(\vec{x}, \omega, \theta) d\omega, & \omega^{(A)}(\vec{x}, \theta) &= A^{(o)} \int_0^\infty \omega A d\omega \\ E^{(o)} &= \omega^{(A)} A^{(o)}, & \bar{v}_i &= (1/E^{(o)}) \int_0^\infty \tilde{E} v_i d\omega, \\ \bar{C}_\theta &= -(1/E^{(o)}) \int_0^\infty \tilde{E} (c_g - \frac{c}{2}) \frac{1}{h} \frac{\partial h}{\partial n} d\omega + \cos\theta \frac{\partial U_1}{\partial n} + \sin\theta \frac{\partial U_2}{\partial n}, & S_1 &= \int_0^\infty \omega S d\omega. \end{aligned}$$

Using Leibniz' rule and rewriting the result, a second equation is obtained:

$$\frac{\partial}{\partial x_i} [A^{(o)} \bar{v}_i] + \frac{\partial}{\partial \theta} (A^{(o)} \bar{C}_\theta) = \frac{1}{\omega^{(A)}} [S_1 - A^{(o)} \bar{v}_i \frac{\partial \omega^{(A)}}{\partial x_i}]. \tag{4}$$

Equations (3) and (4) are the basic equations for HISWA. The source term S_1 is implemented as $(\omega^{(A)}/\sigma^{(A)})S^{(o)}$, where $S^{(o)}$ denotes the change of energy and $\bar{v}_i \partial\omega^{(A)}/\partial x_i$ is interpreted as the change of the frequency

$\omega(A)$ and is prescribed as a function S_ω of the local data. For the inclusion of source terms $S^{(0)}$ and the numerical solution technique is referred to Holthuijsen and Booij (1986).

3.0 EXPERIMENTS

Wave basin

In a wave basin of 26.40 m width and 34 m length a wave generator is available, consisting of 80 flaps which can be driven independently of each other, with a total length of 26.40 m, see Fig. 1. After considering several geometries by numerical investigation, a geometry consisting of a submerged, semi-cylindrical bar on an otherwise horizontal bottom has been chosen, see Fig 1. As a check and for comparison, measurements have also been performed for the case of a submerged, fully cylindrical bar (extending over the whole width of the basin) and for the horizontal bottom situation. The unperturbed water depth is 40 cm. Opposite to the wave generator a wave absorbing gravel beach was made, with a slope of 1:7 and with the waterline at 30 m from the wave board.

Input wave conditions

The input conditions are varied according to the properties of the two-dimensional spectrum $S(f, \theta)$:

- the width of $S(f, \theta)$ in f ;
- the width of $S(f, \theta)$ in θ
- the wave height H_{m0} ;
- the incident wave direction, θ_0 .

We have :

$$S(f, \theta) = E(f) \cdot D(\theta; f),$$

where we took JONSWAP-type spectra $E(f)$ and a $\cos^m(\theta)$ -type directional distribution:

$$E(f) = A_0 \tilde{S}(v) \quad , \quad \tilde{S}(v) = v^{-5} \exp \left[-\frac{5}{4} v^{-4} \right] \gamma(v)$$

$$\gamma(v) = \gamma_0 \exp \left[-\frac{(v-1)^2}{2\sigma} \right] \quad , \quad v = f/f_m,$$

$$A_0 = \alpha_0 g^2 (2\pi)^{-4} f_m^{-5} \quad ; \quad \sigma = 0.07, v < 1; \quad \sigma = 0.09, v > 1$$

and

$$D(\theta; f) = B_2 \cos^m(\theta - \theta_0); \quad -\frac{\pi}{2} \leq \theta - \theta_0 \leq \frac{\pi}{2}$$

$$= 0 \quad ; \quad \text{elsewhere.}$$

$$B_2 = \frac{1}{\sqrt{\pi}} \cdot \frac{\Gamma\left(\frac{1}{2}m + 1\right)}{\Gamma\left(\frac{1}{2}m + \frac{1}{2}\right)}.$$

Here γ_0 is the peak-enhancement factor and m is the exponent of the $\cos^m \theta$ directional distribution.

The input wave conditions, selected in such a way, that some of them are also useful for testing other wave propagation models, are chosen to be

| case | Hs [cm] | Tp [s] | γ_o | m | θ_o [deg] | current meas. |
|------|------------|-----------|------------|----|---------------------|------------------|
| 1 | 5 | 1.25 | 7 | 20 | 0 | - |
| 2 | 10 | 1.25 | 7 | 20 | 0 | - |
| 3 | 10 | 1.25 | 7 | 4 | 0 | - |
| 4 | 10 | 1.25 | 1 | 4 | 0 | - |
| 5 | 10 | 1.25 | 3.3 | 4 | 0 | + |
| 6 | 10 | 1.25 | 7 | 20 | 20 | - |
| 7 | 10 | 1.25 | 3.3 | 4 | 20 | - |
| 8 | 10 | 1.25 | 3.3 | | 0 | + |

Table 3.1 Input conditions.

Measuring devices

The water surface elevation was measured with a resistance type, temperature corrected wave gauge. The relationship between the depth of immersion of the vertical conductor and the output voltage is approximately linear. The deviation from linearity is less than 1% (relative error).

In order to detect the wave directionality, Delft Hydraulics has developed a wave direction meter in which a wave gauge as described above is combined with point measurement of two orbital velocity components in the horizontal plane. The device is a button-type instrument containing two orthogonal electro-magnetic velocity meters (Fig. 2). The measurement range is from -50 to + 50 cm/s. The stability is approximately 1 cm/s, the noise is better than 1 cm/s and the linearity deviation is less than 1% (relative error). The direction of the two velocity components was +45° and -45° to the orthogonal line from the wave generator.

Measurements

At 26 sites, as depicted in Fig. 3, wave height measurements are taken. At seven of these sites directional information is obtained from measurements of the two horizontal velocity components. Because of the large amount of information, and the fact that only three directional measuring devices were available, two repetitions of each run with a different lay-out of the instruments were necessary. The instruments at sites 10 and 15 were kept in place so that the reproducibility of the experiments could be assessed.

Current measurements have been performed for the semi-cylindrical bank situation for the cases 5 and 8, at 81 measuring sites located in a square grid pattern at intervals of 3 m. Three wave direction meters have been used for this purpose, which had to be replaced 26 times so as to cover all positions. At all positions the velocities were measured at half water depth. For three positions the velocities were measured at five different levels so as to obtain some information concerning the vertical structure of the velocity field. Moreover, two wave gauges have been used, which remained at the same place during all tests. At the toe

of the wave damping talus the mean water level was measured at ten different positions by means of a narrow connection tube and gauge-glass.

All cases as given in Table 3.1 have been run for the three different bottom topographies, except the current measurements which have only been performed for the semi-cylindrical bank configuration.

The various measurements are denoted by m_{xy} , where $x = 1, 2, \text{ or } 3$ indicates the geometry (empty basin, cylindrical bank and semi-cylindrical bank respectively) and y gives the measurement condition (1-8) as listed in Table 3.1.

As an example of resulting spectra for m_{35} the spectra $E(f)$ at site 10, close to the wave board and site 28, behind the bar are shown in Figures 4 and 5, together with the target (JONSWAP) spectra, scaled with the spectral peak and the peak frequency. The principal part of the spectrum closely follows the shape of the target spectrum. It is noted, however, that behind the bar a considerable second harmonic spectral peak in $E(f)$ is observed, due to wave breaking over the bar. The variance of this second harmonic peak in the spectrum has been analyzed for seven sites. To characterize this peak we calculated the variance above the frequency $f = 1.4$ Hz, m_{0d2} . For the measurements m_{35} , m_{25} and m_{15} the rate m_{0d2}/m_0 has been given in the next Table, and m_0 is the total variance.

$$m_{0d2} = \int_{1.4}^{3.125} E(f)df, \quad m_0 = \int_0^{3.125} E(f)df.$$

| | site | semi-cyl. me35 | cyl. me25 | empty basin me15 |
|----------|------|-------------------|--------------|------------------------|
| in front | 19 | 20.8 | 19.9 | 18.5 |
| of | 10 | 20.0 | 18.5 | 17.7 |
| bank | 18 | 21.2 | 20.8 | 20.5 |
| on bank | 38 | 21.2 | 20.8 | 20.5 |
| behind | 39 | 37.1 | 51.5 | 17.6 |
| bank | 29 | 43.1 | 52.1 | 18.3 |
| | 28 | 60.9 | 51.0 | 17.8 |

Table 4.1 Values m_{0d2}/m_0 in %.

Inspection of the tabulated results, especially for m_{15} , indicates that the contribution of the second spectral part is approximately 20% in the target spectra, which remains unaffected as the wave field propagates over the horizontal bottom. In the nearly one-dimensional case of wave breaking over the cylindrical bank the second spectral part grows relative to the primary spectral part; the energy densities become approximately equal. In the case of wave breaking over the semi-cylindrical bank the growth of the second spectral part relative to the primary spectral part varies with its position relative to the bank. These results indicate that the concept of one characteristic mean frequency is doubtful in such situations.

5.0 VERIFICATIONS

Boundary conditions and computations

Computations have been performed for all cases in Table 3.1 for both the semi-cylindrical and cylindrical bank geometry. The boundary conditions used as input in the numerical model have been determined from the corresponding measurement series. For the wave height the height H_{m0} at site 10 has been taken ($H_{m0} = 4/m_0$) and for the wave period T the average wave period, T_{m-10} , has been taken, defined as

$$T_{m-10} = m_{-1}/m_0, \quad m_j = \int_0^{\infty} f^j E(f) df$$

The moments m_j have been determined from the measured spectrum.

As the computed wave height behind the bar depends critically on the wave breaking parameter γ , the value for γ has been determined according to the algorithm as given by Battjes and Stive (1985), using T_{m-10} for the wave period. The bottom friction coefficient f_w has been set at 0.01, a reasonable standard value.

Because the sideways boundaries in the mathematical model are dissipative, the wave field close to these boundaries is distorted. Following Dingemans et al. (1984) for the parabolic wave model, a region with an apex of 20 degrees is taken to be a possibly distorted area; this followed also from initial computations with an empty basin. The computational region is now taken to be 50 m wide, instead of 26.40 m, the actual width of the wave basin.

Method of comparison

A relatively large amount of data has been collected, especially since we are dealing with measurements on a grid. The measurement parameters are the wave height H_{m0} , the wave period T_{m-10} , the main wave direction θ and the directional spread σ_θ . In addition to a graphical comparison between measurements and computations, a more objective measure of correspondence was sought. To that end the approach of Willmott (1981, 1984) was adopted, in which a set of statistical measures is used. For all parameters mentioned the following procedure was followed; as an example it is elaborated here for the wave height.

The wave height field as obtained from the measurements m_{xy} is to be compared with that from the corresponding computations; this is done at 26 sites where the wave height is compared with the computed wave height H at that site. In fact, from the computations output is generated in a square of 50 by 50 cm with midpoint the site in question, where 25 wave heights are given (see Sketch 1 below). For the comparison the mean value over the middle 9 points is used; the standard deviations are also computed, but are so low that in fact the wave height at the site alone could equally well have been taken.



Sketch 1

A direct comparison of the H_{m0} and the H values is given by means of a scatter plot, which gives visual information on the correspondence. The statistical parameters recommended by Willmott (1981, 1984) are defined in the following way.

Consider a set of observations $\{O_i\}$ and predictions $\{P_i\}$, $i=1, \dots, n$. Then the mean absolute error, mae, and the root mean square error, rmse, are given by, with $\langle \cdot \rangle$ denoting the averaging operator,

$$\text{mae} = \langle |P_i - O_i| \rangle \quad \text{and} \quad \text{rmse} = [\langle (P_i - O_i)^2 \rangle]^{\frac{1}{2}}.$$

With an ordinary least square regression $\hat{P}_i = a + bO_i$ the systematic and unsystematic part of the rms error, rmses and rmseu, can then be obtained as

$$\text{rmses} = [\langle (\hat{P}_i - O_i)^2 \rangle]^{\frac{1}{2}} \quad \text{and} \quad \text{rmseu} = [\langle (P_i - \hat{P}_i)^2 \rangle]^{\frac{1}{2}}.$$

The potential variance, PE, is given by

$$\text{PE} = \sum_i [|P_i - \langle O_i \rangle| + |O_i - \langle O_i \rangle|]^2$$

and an index of agreement, d, is given as

$$d = 1 - \frac{n \cdot \text{rmse}^2}{\text{PE}}; \quad 0 < d < 1.$$

For $d = 1$ one has perfect agreement and for $d = 0$ none at all.

The parameters $\langle O_i \rangle$, $\langle P_i \rangle$, $s(O_i)$, $s(P_i)$, a , b , mae, rmse, rmses, rmseu and d form a complete set for comparison purposes. Other variables can be derived from this set, see Willmott (1981, 1984). The bias for instance, is given by $(\langle P_i \rangle - \langle O_i \rangle) / \langle O_i \rangle$. It has to be stressed that a single parameter is in most cases not suited for model validation. Notice that these parameters are not scaled, apart from d .

Due to space limitations in the following the attention is restricted to case 5, for the semi-cylindrical bank. This particular choice is motivated by the fact that the conditions of case 5 come close to situations observed in nature and this case is one of the two primary cases around which the parameters are varied (the other one is case 2).

Wave heights

For case 5 a number of numerical model computations was made. One of the initial computations, ve35b, has been performed with starting values $H = 10.42$ cm and $T = 1.17$ s and wave breaking parameter $\gamma = 0.84$. The value of the latter parameter is determined according to the algorithm of Battjes and Stive (1985), so that the model may be considered untuned. The resulting wave heights H at the 26 sites are compared with the corresponding measured H_{m0} values. A scatter plot of these values is given in Figure 6. Notice that the computed wave height values lie mostly below the measured ones; the bias is approximately -7%.

As can be expected in case of the semi-cylindrical bank geometry, a considerable current field is generated by the waves, especially due to wave breaking on the bar. Because the mathematical model also gives the

driving forces (in fact the gradients of the radiation stress components) for subsequent use in current models, such a wave driven current computation has been carried out and the resulting current field has been used in a second computation, ve35bs, in order to account for effects of current refraction on the wave field. The current field of a closely related computation, ve35a, where $\gamma = .80$ instead of $.84$ in ve35b, has been given in Fig. 7 and the stream function is given in Fig. 8. The resulting scatter plot of the pairs of wave heights at the sites is shown in Fig. 9. It is clear upon comparison of Figures 6 and 9 that inclusion of wave driven currents gives a closer correspondence between computed and measured wave heights. The bias has been reduced from approximately -7% to approximately -2%.

Because the wave generated current field has also been measured for case 5 for the semi-cylindrical bank geometry in 81 points 3 m apart, see Fig. 10, the measured current field can also be used for the wave propagation computations. The result of such a computation, ve35s1, has been given in the scatter plot of Fig. 11.

The statistical parameters for the computations ve35b, ve35bs and ve35s1 are given in the Table 5.1 below. For comparison the results for the fully cylindrical bank, computation ve25 ($H = 10.23$ cm, $T = 1.17$ s, $\gamma = 0.83$), are also included; H_c denotes the computed wave heights.

| | ve35b | ve35bs | ve35s1 | ve25 |
|-------------|-------|--------|--------|-------|
| <Hm0> [cm] | 8.79 | 8.79 | 8.79 | 6.97 |
| <Hc> [cm] | 8.22 | 8.65 | 8.55 | 6.91 |
| s(Hm0) [cm] | 1.76 | 1.76 | 1.76 | 2.52 |
| s(Hc) [cm] | 2.01 | 1.76 | 1.79 | 2.52 |
| a [cm] | -1.14 | 0.48 | -0.09 | -0.03 |
| b - | 1.06 | 0.93 | 0.98 | 1.00 |
| mae [cm] | 0.72 | 0.53 | 0.36 | 0.22 |
| rmse [cm] | 0.92 | 0.66 | 0.50 | 0.28 |
| rmse [cm] | 0.59 | 0.19 | 0.24 | 0.06 |
| rmseu [cm] | 0.71 | 0.63 | 0.43 | 0.27 |
| d - | 0.94 | 0.96 | 0.98 | 1.00 |

Table 5.1 Statistical parameters for wave height, over 26 sites.

These figures show that the correspondence between computed and measured wave heights becomes better with increasing accuracy of the current field. Concentrating on the mae and rmse deviation measures a continuous reduction is seen to occur from left to right in the Table. Whereas the accuracy of the wave height prediction in case ve35b (no current refraction) is already satisfactory (bias -6.6% and rmse = 10.5%), a large part of these deviations is due to the neglect of the wave-induced current field.

Taking the measured current field into account in the wave propagation computation, one has bias = -2.8% and rmse = 5.7%; as scaling parameter the value <Hm0> has been used. Considering the systematic part of the rmse deviation, rmse, it is seen that tuning is possible for better correspondence because the contribution to the mean square error due to systematic deviations is still 24% of the total mean square error; in

the optimal case this value should approach zero. It is stressed that the parameter setting has not been tuned to the measurements, only the boundary condition for the wave height and the wave period have been taken from the values at site 10, situated close to the middle of the wave board. Furthermore one single wave height was taken along the boundary, whereas, in the measurements some variation was obtained, primarily due to current refraction. It is noted furthermore that the nearly one-dimensional case, ve25, gives indeed the best results.

Wave periods

In order to be able to compare the computed wave periods, T_c , with the measured ones, it is necessary to derive the wave periods T_{m-10} from the measured wave spectra. This is done only for the 7 sites on which also the wave direction is available. The statistical parameters then become:

| | | ve35b | ve35bs | ve35s1 | ve25 |
|----------------------------|-----|-------|--------|--------|-------|
| $\langle T_{m-10} \rangle$ | [s] | 1.11 | 1.11 | 1.11 | 1.12 |
| $\langle T_c \rangle$ | [s] | 1.07 | 1.05 | 1.05 | 0.95 |
| $s(T_{m-10})$ | [s] | 0.08 | 0.08 | 0.08 | 0.06 |
| $s(T_c)$ | [s] | 0.11 | 0.13 | 0.13 | 0.22 |
| a | [s] | -0.31 | -0.25 | -0.45 | -2.41 |
| b | - | 1.25 | 1.17 | 1.35 | 2.99 |
| mae | [s] | 0.05 | 0.07 | 0.07 | 0.19 |
| rmse | [s] | 0.07 | 0.10 | 0.10 | 0.24 |
| rmse _s | [s] | 0.04 | 0.06 | 0.07 | 0.20 |
| rmse _u | [s] | 0.06 | 0.08 | 0.07 | 0.13 |
| d | - | 0.85 | 0.72 | 0.76 | 0.41 |

Table 5.2 Statistical parameters for wave period, over 7 sites.

Compared with the results of the wave heights, the prediction of the wave periods is not so good. In order to check the deviations more accurately point by point comparisons are made, of which the results are given in the next Table. Here δ is the relative error $\delta = (T_c - T_{m-10})/T_{m-10}$.

| site | ve35b | | | ve25 | | |
|------|-------|------------|------------|-------|------------|------------|
| | T_c | T_{m-10} | δ % | T_c | T_{m-10} | δ % |
| 19 | 1.169 | 1.148 | 1.8 | 1.182 | 1.164 | 1.55 |
| 10 | 1.169 | 1.170 | -0.10 | 1.182 | 1.183 | -0.05 |
| 18 | 1.169 | 1.164 | 0.42 | 1.182 | 1.160 | 1.94 |
| 38 | 1.021 | 1.168 | -12.25 | 0.770 | 1.162 | -33.74 |
| 39 | 1.093 | 1.092 | 0.12 | 0.771 | 1.075 | -28.30 |
| 29 | 1.000 | 1.069 | -6.47 | 0.771 | 1.054 | -26.87 |
| 28 | 0.877 | 0.966 | -9.18 | 0.772 | 1.061 | -27.24 |

Table 5.3 Computed (T_c) and measured (T_{m-10}) wave periods at 7 sites.

As wave period changes are best checked with the fully cylindrical bank topography, the result of ve25 is more pertinent to this case than is the result of ve35b. In fact, the change in frequency can be better studied in a wave flume because directional spreading is not of importance

here (highly dissipative waves). It is seen that behind the bar the computed wave periods are about 30% too low. That the figures for ve35b are much better is due to the fact that, because of refraction, a considerable amount of "unbroken" waves reach the region behind the bar; this is especially true for the case ve35b, where no current refraction effects are included.

One should be aware of the simple adjustment of the wave periods, via some similarity approach, taking a very simplified spectral shape. It is clearly necessary to investigate the wave period adjustment further.

Wave directions

The measured values θ_m are determined as follows. At each spectral frequency (of a total of 128) the wave direction θ is determined from the Fourier coefficients of the directional function by

$$\theta(f) = b_1(f)/a_1(f)$$

and the directional spread σ_0 follows as

$$\sigma_0 = [2\{1 - (a_1^2 + b_1^2)\}]^{\frac{1}{2}}$$

The values θ_m follow from a simple average of the 10 values around the spectral peak frequency. The inaccuracy of θ_m is estimated to be up to about 4° , due to inaccuracy in the placing of the measuring device and the inaccuracy of the data.

| site | me35 θ_m | ve35b θ_c | ve35bs θ_c | ve35s1 θ_c | me25 θ_m | ve25 θ_c |
|------|--------------------|---------------------|----------------------|----------------------|--------------------|--------------------|
| 19 | -5.6 | 0 | -0.11 | 0.69 | -4.14 | 0 |
| 10 | 1.34 | 0 | -0.16 | -0.06 | 2.47 | 0 |
| 18 | -3.63 | 0 | -0.16 | 0.15 | -0.29 | 0.01 |
| 38 | -13.88 | -33.10 | 4.98 | -13.18 | -4.38 | 0.22 |
| 39 | -3.37 | -19.16 | -4.73 | -1.50 | -7.54 | 0.22 |
| 29 | -9.64 | -22.74 | 0.01 | -2.86 | -6.35 | -0.02 |
| 28 | 2.32 | -21.00 | -0.19 | -7.54 | 1.06 | -0.56 |

Table 5.4 Measured (θ_m) and computed (θ_c) wave directions.

The site 38 at the tip of the semi-cylindrical bank is the most sensitive one for checking the wave directions (in fact, the point was chosen because of this). It is seen from Table 5.4 that in this situation inclusion of current refraction is of utmost importance to a good prediction of wave directions. This can also be made clear visually from the Figures 12 and 13 where the vector plots of wave heights and directions are shown for the cases ve35a and ve35s1. Total refraction is much reduced when accounting for the wave driven current field. Especially the circulation cell near the head of the bar is important here. In the calculated current field as used in ve35bs this cell was apparently not calculated accurately enough, because the error in the calculated predominant wave direction remained about 20 degrees, but now in the opposite direction.

The values of the statistical parameters for the wave direction θ are:

| | ve35b | ve35bs | ve35s1 |
|--------------------------|-------|--------|--------|
| $\langle\theta_m\rangle$ | -4.6 | -4.6 | -4.6 |
| $\langle\theta_c\rangle$ | -13.7 | -0.1 | -3.5 |
| $s(\theta_m)$ | 5.7 | 5.7 | 5.7 |
| $s(\theta_c)$ | 13.6 | 2.8 | 5.1 |
| a | -7.9 | -1.3 | -1.6 |
| b | 1.3 | -0.3 | 0.4 |
| rmse | 14.0 | 8.5 | 5.4 |
| rmse _s | 9.2 | 8.2 | 3.4 |
| rmse _u | 10.6 | 2.2 | 4.4 |
| d | 0.53 | 0.33 | 0.69 |

Table 5.5 Statistical parameters for wave directions.

It is seen from Tables 5.4 and 5.5 that value of the index of agreement d is quite low in all cases, as also follows from the linear regression coefficient b .

6.0 CONCLUSIONS

For wave height prediction the numerical model performs well: without taking the wave-generated current field into account the bias is -6.6% and the rms error is 10.5%. Taking the current field into account these values are -2.8% and 5.7% respectively. Notice that these values are obtained without any tuning of the model, i.e. the parameters are chosen beforehand according to known prescriptions, derived from other model investigations, where, moreover, a fixed frequency was chosen. Especially for the wave breaking parameter γ there are indications, also obtained from other models, that it should be chosen somewhat higher; this would result in a smaller negative, or positive, bias. As the figures are based on all 26 values, and values in front of the bank are of course much better, the accuracy is somewhat less than apparent from the given figures. Taking into account the 17 sites lying on and behind the bank, the result is bias = -7.8 versus -3.2% and rmse = 11.1 versus 5.1%.

For a good prediction of the principal wave direction the inclusion of the wave-generated current field is essential. The prediction of the wave period is less satisfactory, the decrease in T is too fast. The modelling of the change in frequency is too simple; a very schematized spectral shape is assumed and, moreover, the assumed similarity of spectral shapes is seen not to be valid in strong dissipation zones. The effect of wave breaking on the spectral shape is the loss of energy on the low frequency part and the generation of higher harmonics in the spectrum, see Figures 4 and 5. It can also happen that wave breaking is so strong that the wave energy in the original frequency band has totally disappeared and that only the higher harmonic peak in the spectrum remains; an example of this behaviour has been given in Figures 17 and 18 of Dingemans et al. (1984) for field measurements in the Haringvliet region, in the Rhine-Meuse estuary. It is necessary to model the transfer of energy to higher harmonics in the spectrum in order to be able to obtain a good prediction of characteristic wave period due to breaking of waves in shallow water.

The wave-induced current field prediction is quite good. Inclusion of such current fields has been shown to be necessary in some situation so as to obtain more accurate wave height predictions in shallow water regions. The modelling of wave and current fields, possible via an iterative computation procedure, needs further investigation. This may be important for coastal models with waves and tides, especially where the interaction between bottom changes and waves and currents is a very sensitive process.

7.0 REFERENCES

- Battjes, J.A. and M.J.F. Stive, (1985).** Calibration and verification of a dissipation model for random breaking waves. *J. Geophysical Res.* 90 (C5), Sept. 1985 pp. 9159-9167.
- Booij, N., L.H. Holthuijsen and T.H. Herbers, (1985).** A numerical model for wave boundary conditions in port design. *Int. Conf. on Numerical and Hydraulic Modelling of Ports and Harbours*, Birmingham, England, April 1985, pp. 263-268.
- Dingemans, M.W., M.J.F. Stive, A.J. Kuik, A.C. Radder and N. Booij, (1984).** Field and laboratory verification of the wave propagation model CREDIZ. *Proc. 19th Conf. on Coastal Engng*, Houston, 1984 pp. 1178-1191.
- Holthuijsen, L.H. and N. Booij, (1986).** A grid model for shallow water waves. *Proc. 20th Conf. on Coastal Engng*, Taipei 1986.
- Mynett, A.E., J. Bosma and P. van Vliet, (1984).** Effects of directional seas in coastal regions. *Symposium on Description and Modelling of Directional Seas*, Paper B7, Lyngby, Denmark.
- Willmott, C.J., (1981).** On the validation of models. *Physical Geography* 2(2), 1981 pp. 219-232.
- Willmott, C.J., (1984).** On the evaluation of model performance in physical geography. In: *Spatial statistics and models* (Eds. G.L. Gaile and C.J. Willmott), pp. 443-460, Reidel 1984.

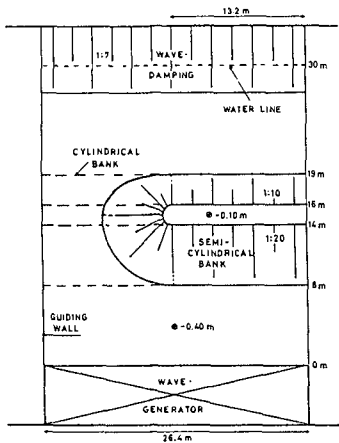


Fig. 1 Wave basin lay out

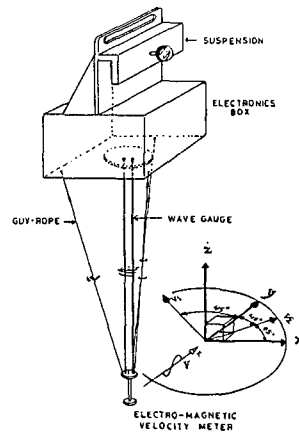


Fig. 2 Wave direction meter

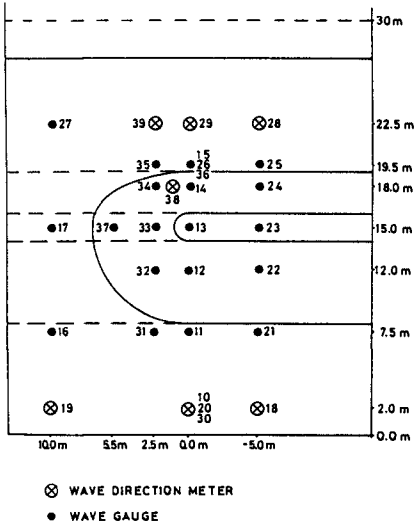


Fig. 3 Measuring positions

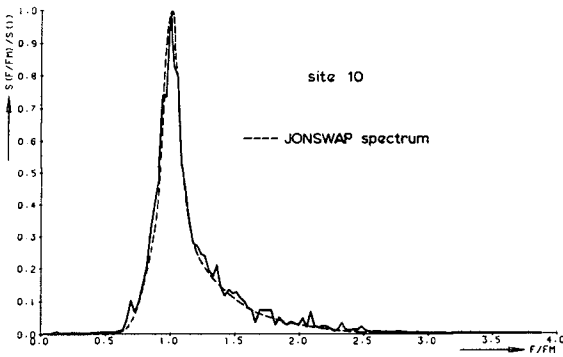


Fig. 4 Spectrum at site 10

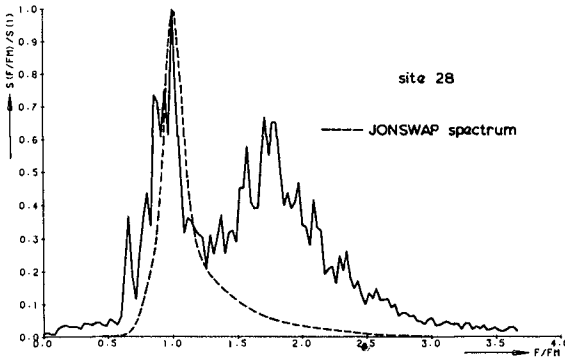


Fig. 5 Spectrum at site 28

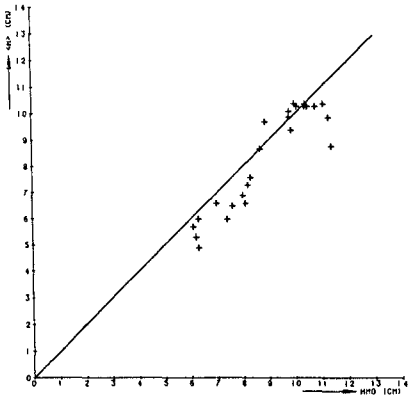


Fig. 6 Scatter plot wave heights, ve35b

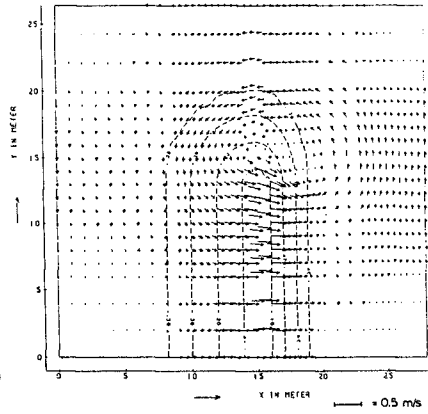


Fig. 7 Current vectors, ve35a

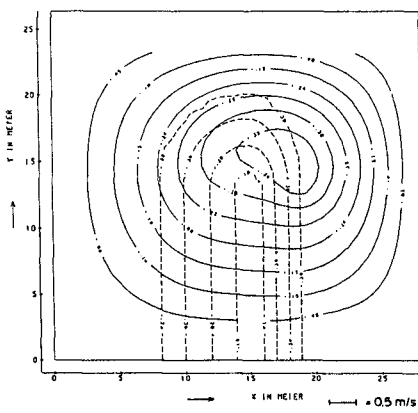


Fig. 8 Stream function, ve35a

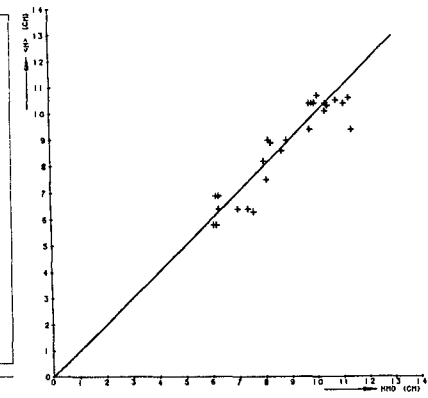


Fig. 9 Scatter plot wave heights, ve35bs

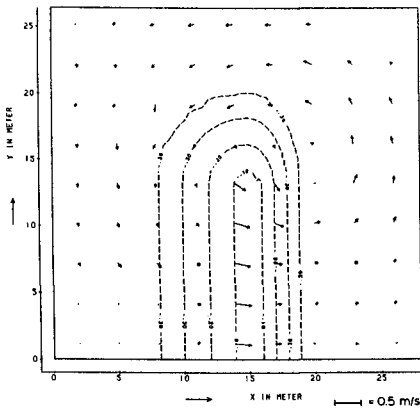


Fig. 10 Measured current vectors, me35

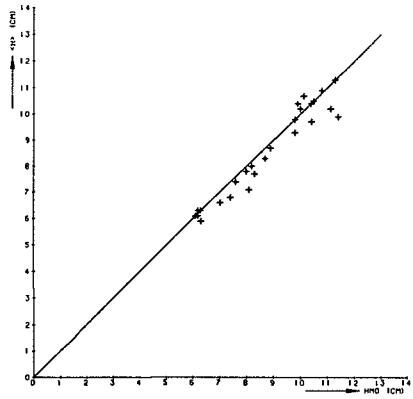


Fig. 11 Scatter plot wave heights, ve35sl

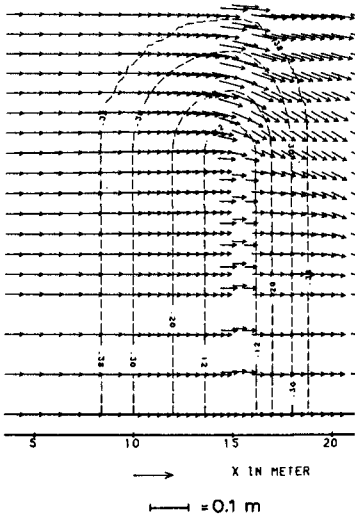


Fig. 12 Vector plot wave heights and directions, ve35a

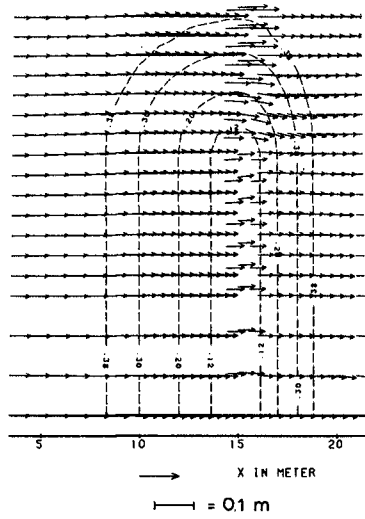


Fig. 13 Vector plot wave heights and directions, ve35sl